



Quantitative Imaging of Exotic Antiferromagnetic Spin Cycloids in BiFeO₃ Thin Films

Hai Zhong, Aurore Finco, Johanna Fischer, Angela Haykal, Karim Bouzehouane, Cécile Carrétéro, Florian Godel, Patrick Maletinsky, Mathieu Munsch, Stéphane Fusil, et al.

► To cite this version:

Hai Zhong, Aurore Finco, Johanna Fischer, Angela Haykal, Karim Bouzehouane, et al.. Quantitative Imaging of Exotic Antiferromagnetic Spin Cycloids in BiFeO₃ Thin Films. *Physical Review Applied*, 2022, 17, 10.1103/physrevapplied.17.044051 . hal-03656679

HAL Id: hal-03656679

<https://hal.science/hal-03656679>

Submitted on 2 May 2022

HAL is a multi-disciplinary open access archive for the deposit and dissemination of scientific research documents, whether they are published or not. The documents may come from teaching and research institutions in France or abroad, or from public or private research centers.

L'archive ouverte pluridisciplinaire **HAL**, est destinée au dépôt et à la diffusion de documents scientifiques de niveau recherche, publiés ou non, émanant des établissements d'enseignement et de recherche français ou étrangers, des laboratoires publics ou privés.

Quantitative Imaging of Exotic Antiferromagnetic Spin Cycloids in BiFeO₃ Thin Films

Hai Zhong¹, Aurore Finco¹, Johanna Fischer¹, Angela Haykal¹, Karim Bouzehouane³, Cécile Carrétéro³, Florian Godel³, Patrick Maletinsky⁴, Mathieu Munsch¹, Stéphane Fusil³, Vincent Jacques², and Vincent Garcia^{3,*}

¹Qnami AG, Hofackerstrasse 40 B, CH-4132 Muttenz, Switzerland

²Laboratoire Charles Coulomb, Université de Montpellier and CNRS, 34095 Montpellier, France

³Unité Mixte de Physique, CNRS, Thales, Université Paris-Saclay, 91767 Palaiseau, France

⁴Department of Physics, University of Basel, Klingelbergstrasse 82, Basel CH-4056, Switzerland



(Received 12 January 2022; accepted 1 April 2022; published 26 April 2022)

BiFeO₃ is a rich room-temperature multiferroic material in which noncollinear antiferromagnetic spin cycloids can be deterministically controlled by an electric field through the magnetoelectric interaction, opening perspectives for low-power reconfigurable antiferromagnetic spintronics. Using a commercial scanning nitrogen-vacancy (N-V) magnetometer, we are able to image two different types of spin cycloids stabilized in strain-engineered BiFeO₃ epitaxial thin films. We show that, in these samples harboring two ferroelectric variants, each ferroelectric domain is coupled to a single spin cycloid, giving rise to a zigzag magnetic pattern. These ferroelectric domains can be manipulated at the local scale by piezoresponse force microscopy, allowing the design of micron-sized single domains. Thanks to its coupled optical microscope and fast-imaging capabilities, the scanning N-V magnetometer enables a quick repositioning in such areas of interest. Finally, quantitative imaging on single ferroelectric domains provides insights into the physical parameters of each spin-cycloid type and their impact on the magnetic-stray-field measurements.

DOI: 10.1103/PhysRevApplied.17.044051

I. INTRODUCTION

In the bulk, BiFeO₃ crystallizes in the *R3c* space group and is ferroelectric at room temperature ($T_C = 1100$ K) with a large polarization ($100 \mu\text{C}/\text{cm}^2$) pointing along one of the eight possible [111] pseudocubic directions [1]. Moreover, this material is antiferromagnetic below $T_N = 640$ K with an additional antisymmetric magnetoelectric interaction that leads to an incommensurate antiferromagnetic spin cycloid with a period of 62–64 nm [2,3]. A second Dzyaloshinskii-Moriya magnetic interaction (DMI) is triggered by the antiferrodistortive tilts of oxygen octahedra, which gives rise to a spin-density wave developing perpendicularly to the cycloidal plane [4]. This spin cycloid can be destroyed either by strong magnetic fields [5] or by hydrostatic pressure [6], resulting in a canted *G*-type antiferromagnetic state. The ferroelectric and antiferromagnetic orders are coupled in this room-temperature multiferroic material [3,7], which stimulates intensive research on epitaxial thin films of BiFeO₃ over the last two decades [8].

At first, the antiferromagnetic cycloid was believed not to exist in thin films due to epitaxial strain, resulting in a canted *G*-type antiferromagnetic order [9,10]. Nevertheless, neutron diffraction revealed that partially relaxed thick BiFeO₃ layers (>200 nm) possess a spin-cycloidal state as in the bulk material [11]. Later, Mössbauer and Raman spectroscopy studies showed that even epitaxial thin films of BiFeO₃ (<60 nm) harbored a bulk-like spin cycloid for low compressive strain, while large compressive and tensile strain favored a canted antiferromagnetic state [12]. Recently, real-space imaging of the antiferromagnetic spin textures using scanning nitrogen-vacancy (N-V) magnetometry demonstrated unambiguously the existence of the spin cycloid in 30-nm-thick films of BiFeO₃ with a one-to-one correspondence between cycloidal and ferroelectric domains [13]. Thanks to magnetoelectric coupling, the electric field allows a deterministic control of spin cycloids, opening a path for low-power reconfigurable antiferromagnetic spintronics. Furthermore, these noncollinear antiferromagnetic textures of BiFeO₃ can be controlled by the combination of epitaxial strain and electric field [14]. Notably, for low tensile strain, a different kind of spin cycloid can be stabilized, as inferred from fitting Mössbauer data. Combining high-quality strain-engineered epitaxial thin films with highly

*vincent.garcia@cnrs-thales.fr

sensitive scanning N-V magnetometry, the magnetic versus strain phase diagram is investigated and demonstrated to be richer than previously depicted [12]. Indeed, using DyScO₃(110) or TbScO₃(110) substrates, imposing low compressive strain, favors the bulklike (type I) cycloid with [1̄10] propagation vectors restricted to the film plane of BiFeO₃. For large compressive strain [on SrTiO₃(001)] or small tensile strain [on GdScO₃(110)], the exotic type-II cycloid is stabilized with propagation vectors along the [2̄11] and [12̄1] directions, i.e., as close as possible to the film plane of BiFeO₃. Finally, large tensile strain [on SmScO₃(110)] seems to destroy the cycloid and favor pseudocolinear canted antiferromagnetic domains.

Here, using a commercial scanning N-V magnetometer, we explore the antiferromagnetic textures of BiFeO₃ thin films, displaying a self-organized ferroelectric stripe-domain pattern. The films are grown on (110) DyScO₃ and SmScO₃ substrates, imposing compressive and tensile strain, respectively. Surprisingly, in both cases, the periodic zigzag magnetic pattern attests to the presence of spin cycloids. This observation pushes back the borders of the spin-cycloid stability domain in the magnetic versus strain phase diagram. We clearly distinguish the presence of the bulklike (type I) and exotic (type II) spin cycloids for films grown under compressive and tensile strain, respectively. Owing to its excellent mechanical and thermal stability, the scanning N-V magnetometer allows the mapping of large areas, including single ferroelectric domains previously written *ex situ* using piezoresponse force microscopy. Finally, quantitative maps in single ferroelectric domains containing either type I or type II spin cycloids allow us to extract the different physical parameters at play and to reveal a small deviation of the type-II-cycloid propagation vector with respect to the expected one.

II. SCANNING N-V MAGNETOMETER AND PROBE CALIBRATION

The antiferromagnetic spin textures of the BiFeO₃ samples are imaged using a commercial scanning N-V magnetometer (ProteusQ™, Qnami AG) operated under ambient conditions, with key components conceptionally sketched in Fig. 1(a). In our setup, the scanning tip is a commercial all-diamond probe with a single N-V defect at its apex integrated on a quartz tuning fork (Quantilever™ MX, Qnami AG). The diamond tip is integrated into a tuning-fork-based atomic force microscope combined with a confocal microscope optimized for single N-V defect spectroscopy.

The N-V center is initialized by an integrated green-laser source (continuous wave with a wavelength of 515 nm, focused onto the scanning tip via the 100× magnification and NA = 0.7 top objective) and the photoluminescence (PL) signal emitted from the N-V center is collected via the same objective, which is part of the confocal optical

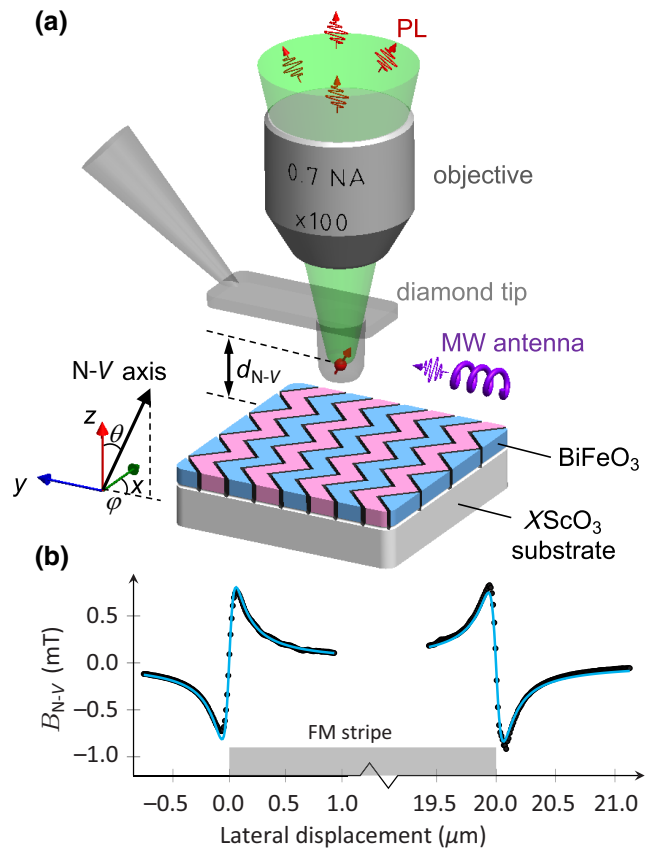


FIG. 1. (a) Working principle of the Qnami ProteusQ scanning N-V magnetometer. Single N-V defect (red arrow) localized at the apex of a diamond tip is scanned above BiFeO₃ thin film grown on $X\text{ScO}_3$ ($X = \text{Dy}, \text{Sm}$) substrates. Near-field microwave (MW) delivery line is used to excite the electron-spin resonance of the N-V center. Objective placed above the tip is used to collect the photoluminescence of the N-V defect under continuous green-laser excitation. (b) Calibration of the N-V-to-sample distance, $d_{\text{N}-V}$, by measuring a line profile of the magnetic stray field produced by the edges of a 20- μm -wide out-of-plane magnetized ferromagnetic (FM) Co-Fe-B stripe of 0.8 nm thickness and 1.2 MA m⁻¹ magnetization [16]. Fit (blue line) gives $d_{\text{N}-V} = (62.7 \pm 2)$ nm, $\theta = 60.1^\circ \pm 0.5^\circ$, $\varphi = -90.2^\circ \pm 1^\circ$, considering the topography of the ferromagnetic wire and fitting to data from both edges simultaneously.

module of the instrument. A near-field microwave delivery line in proximity to the N-V tip is used to excite the N-V spin resonance for magnetometry [Fig. 1(a)]. Magnetic fields emanating from the sample are detected by recording the Zeeman shift of the N-V defect's electronic spin sublevels through optical detection of the electron-spin resonance (ESR) [15]. The magnetic field component projected along the N-V quantization axis is determined by measuring the splitting of the ESR spectra, via the simple relation of $B_{\text{N}-V} = \Delta\nu/2\gamma_{\text{N}-V}$, where $\gamma_{\text{N}-V} = 28$ GHz/T is the gyromagnetic ratio of the N-V center, and $\Delta\nu$ is the splitting of the ESR spectra.

Here, we use two different N-V imaging modes. For a fast sample overview in a larger scan area [as discussed later in Fig. 3(d)], we use “single iso-B scans” with a typical pixel integration time of tens of milliseconds (20 ms/pixel). In such images, dark contours indicate the local isomagnetic field lines, where the N-V spin transition is in resonance with the preselected microwave frequency, ν_{iso} [15]. For detailed quantitative studies in the local regions of interest, we use a full quantitative imaging mode by recording the full N-V ESR spectra at each pixel, with typical integration times of a few seconds (4.5 s/pixel).

We calibrate the N-V-to-sample distance, $d_{\text{N-V}}$, following the procedure described in Ref. [17], by mapping the magnetic stray field generated above the edges of a uniformly magnetized ferromagnetic Co-Fe-B thin-film stripe with out-of-plane anisotropy (see sample details in Ref. [16]). We first estimate roughly the polar angle, θ , and the azimuthal angle, φ , which determine the N-V-center orientation [Fig. 1(a)] by means of a permanent magnet, before fitting the analytical expression for the stray-field profile to experimental data, while leaving $d_{\text{N-V}}$, θ , and φ as free parameters [Fig. 1(b)]. Because the ferromagnetic stripe is 20 μm wide, we measure the up and down steps separately using the full quantitative mode, but perform the fit on both sides simultaneously. This calibration allows us to achieve a quantitative analysis of our data, as illustrated in detail in Sec. IV.

While the incommensurate antiferromagnetic spin cycloid is not expected to produce any stray field because of full spin compensation at (001) surfaces, the uncompensated magnetic moment, m_{DM} , of the spin-density wave produces a small stray field in the few tens of μT

range [18]. The scanning N-V magnetometer sensitivity ($\sim 1 \mu\text{T}/\sqrt{\text{Hz}}$) allows the mapping of such a stray field and the visualization of the long-range periodicity of the spin cycloid.

III. IMAGING AS-GROWN AND ELECTRICALLY CONTROLLED SPIN CYCLOIDS

BiFeO_3 thin films are grown by pulsed-laser deposition on $\text{DyScO}_3(110)_o$ and $\text{SmScO}_3(110)_o$ (o stands for orthorhombic) substrates, using a KrF excimer laser (248 nm). Prior to growth, the scandate substrates are annealed under an oxygen flow for 3 h at 1000 °C. On each substrate, an oxide buffer electrode of SrRuO_3 is grown at 650 °C under an oxygen pressure of 0.2 mbar. BiFeO_3 is grown at the same temperature under an oxygen pressure of 0.36 mbar. The samples are then cooled to room temperature under 300 mbar oxygen pressure. The film thicknesses are determined using x-ray reflectivity and cross-checked with Laue fringes in the $2\theta-\omega$ diffraction patterns. We estimate the thickness of SrRuO_3 to be around 5 nm for both samples. The thicknesses of BiFeO_3 are estimated to be 33 and 54 nm for films grown on DyScO_3 and SmScO_3 , respectively. Using advanced x-ray diffraction with reciprocal space maps [14], we deduce that the BiFeO_3 thin films are (001) oriented with only two ferroelastic variants, as imposed by the symmetry of the (110) $_o$ orthorhombic substrates [19]. A suitable set of reciprocal space maps allows us to estimate the in-plane epitaxial strain as -0.3% (on DyScO_3) and $+0.5\%$ (on SmScO_3).

Using piezoresponse force microscopy (PFM), we are able to map the ferroelectric domains in these films.

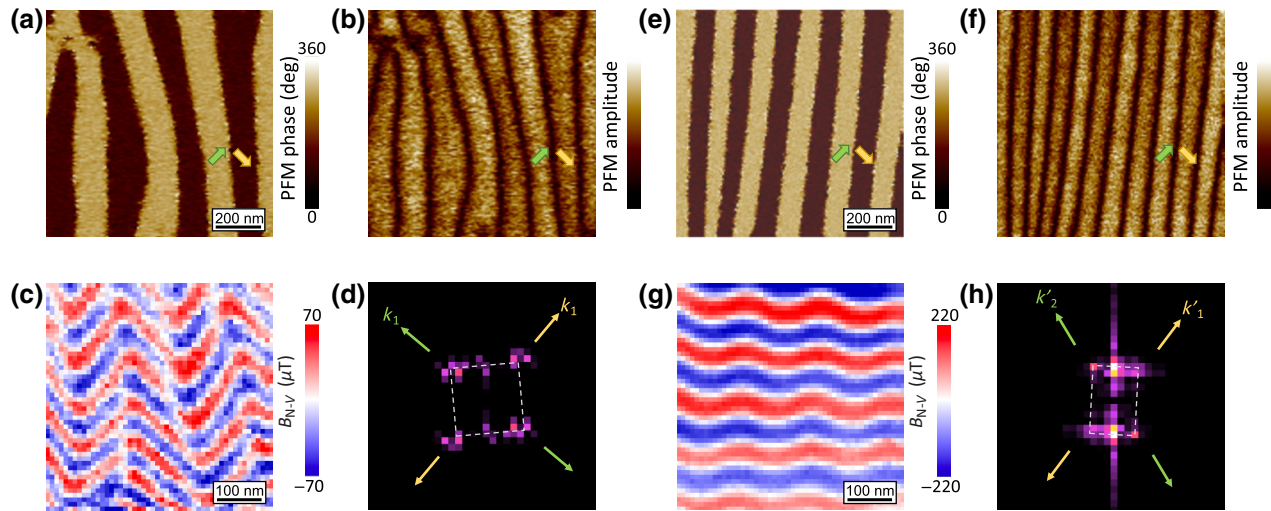


FIG. 2. In-plane PFM (a) phase and (b) amplitude images of the BiFeO_3 thin film grown on $\text{DyScO}_3(110)_o$. (c) Quantitative scanning N-V magnetometry image on the same sample and (d) corresponding FT. In-plane PFM (e) phase and (f) amplitude images of the BiFeO_3 thin film grown on $\text{SmScO}_3(110)_o$. (g) Quantitative scanning N-V magnetometry image on the same sample and (h) corresponding FT. Green and yellow arrows indicate the two in-plane polarization directions (wide arrows) and the corresponding k propagation vectors of the spin cycloids (thin arrows).

Figures 2(a) and 2(e) display typical in-plane PFM phase images showing striped domains aligned along the [001]_o direction of the substrates, with periodic 71° domain walls for both samples. The corresponding in-plane PFM amplitude images [Figs. 2(b) and 2(f)] show a homogeneous bright signal that vanishes only at the domain walls. Notably, the out-of-plane PFM phase signal (not shown) is homogeneous for both samples and indicates polarization pointing downward, i.e., towards the SrRuO₃ electrode. Hence, from one domain to another, the in-plane component of polarization rotates by 90° [as sketched by the green and yellow arrows in Figs. 2(a), 2(b), 2(e), and 2(f)] and the out-of-plane component of polarization remains the same.

Scanning N-V magnetometry images are collected on both samples. Figure 2(c) displays the magnetic-stray-field image produced by the striped-domain structure of BiFeO₃ grown on DyScO₃. As previously reported [13,14], the stray field evolves periodically, indicating the presence of a spin cycloid. In addition, the propagation direction of the spin cycloid rotates periodically with a period matching the ferroelectric one, giving rise to a magnetic zigzag pattern. The rotation angle between each propagation vector is estimated to be 90°, as expected for a type-I cycloid with a [110] propagation vector in each ferroelectric domain, i.e., systematically in the film plane. The Fourier transform (FT) of the image [Fig. 2(d)] confirms the presence of two orthogonal propagation vectors, defining a square pattern with an estimated period of (66 ± 10) nm. Indeed, on the film-plane projection, each k_1 propagation vector makes an angle of 90° with the polarization. For BiFeO₃ thin films grown on SmScO₃ substrates, a regular zigzag pattern is also observed [Fig. 2(g)]. This is surprisingly different from previous observations in which a transition to a canted antiferromagnetic state was concluded [14]. While the epitaxial strain is similar, we believe that the films presented here possess a higher crystalline quality than that in our previous report, as visible from the high degree of ferroelectric order [Figs. 2(e) and 2(f)]. Such a self-ordered ferroelectric pattern is indeed computed as being the ground state of BiFeO₃ thin films [20]. In contrast to BiFeO₃ films grown on DyScO₃, the rotation of the propagation vector is no longer 90° from one domain to another. From the FT [Fig. 2(h)], we estimate this angle to be 112° ± 10° with a surface period of (88 ± 10) nm. This rectangular pattern in the FT is consistent with a type-II cycloid, where k'_1 and k'_2 propagation vectors are aligned along the [211] and [121] directions, respectively, as previously observed for lower tensile strain (BiFeO₃ grown on GdScO₃) [14]. The intrinsic period of this type-II cycloid is calculated to be (80 ± 10) nm, using a geometrical $\sqrt{5}/6$ factor [14].

Figure 3(a) displays an out-of-plane PFM phase image in which the homogeneous bright contrast stands for the initial downward-polarization state. Two dark $2 \times 2 \mu\text{m}^2$

squares are written by scanning the grounded conducting tip of the PFM at 45° from the [001]_o direction while applying a positive dc bias (about twice the coercive bias) on the SrRuO₃ bottom electrode, which reverses the polarization to upward variants. The different directions of the slow-scan axis of the atomic force microscope enable us to control the in-plane directions of polarization thanks to the so-called trailing field [21,22], as confirmed by the two different in-plane PFM phase signals in the squares of Fig. 3(b). Using gold markers defined by optical lithography and lift-off, we are able to relocate these areas of interest with the optical microscope of the scanning N-V magnetometer. To start with, a fast (typically a few tens of milliseconds per pixel) $2 \times 2 \mu\text{m}^2$ single iso- B fluorescence scan is displayed in Fig. 3(d), and its location with respect to the ferroelectric domains is shown by the red squares in Figs. 3(a)–3(c). From this large scanned area, we clearly distinguish the virgin zigzag pattern of the magnetic stray field inferred from the striped ferroelectric domains and areas containing only a single spin cycloid. Then, the high stability of the microscope allows us to scan selected areas in a full quantitative mode [typically a few seconds per pixel, see Figs. 3(e)–3(g)]. In addition to the virgin state [Fig. 3(e)], two magnified areas are selected: in a single ferroelectric domain [Fig. 3(f)] and at the domain wall between two single domains [Fig. 3(g)]. In the single ferroelectric domain [Fig. 3(f)], a regular periodic magnetic signal is observed with a single k_1 propagation vector oriented 90° from the in-plane component of polarization [Fig. 3(b)]. Interestingly, in the area of the 109° tail-to-tail ferroelectric domain wall [Fig. 3(g)], the magnetic pattern shows 90° rotation of the propagation vector of the spin cycloid, with an associated high magnetic stray field. This suggests that the charged 109° ferroelectric domain-wall structure splits into more stable 71° neutral domain walls. Vectorial PFM investigations on similar artificial 109° domain walls (not shown) confirm the presence of nanodomains forming 71° domain walls, thus avoiding the formation of charged domain walls. In the putative case of charged 109° domain walls, we would expect the N-V image to show only the same in-plane component of the k vector, including possible stitching peculiarities.

IV. QUANTITATIVE ANALYSIS IN SINGLE SPIN CYCLOIDS

Figure 4 summarizes the influence of the epitaxial strain on the cycloidal period in (001)-oriented BiFeO₃ thin films. The different types of spin cycloids are color coded as a guide to the eye. For films under low compressive and tensile strain between -0.35% and +0.05%, despite the change from type-I to type-II cycloids, the period remains very close to that of bulk BiFeO₃. Interestingly, for films under higher strain ($\leq -1.35\%$ or $\geq +0.5\%$), which are

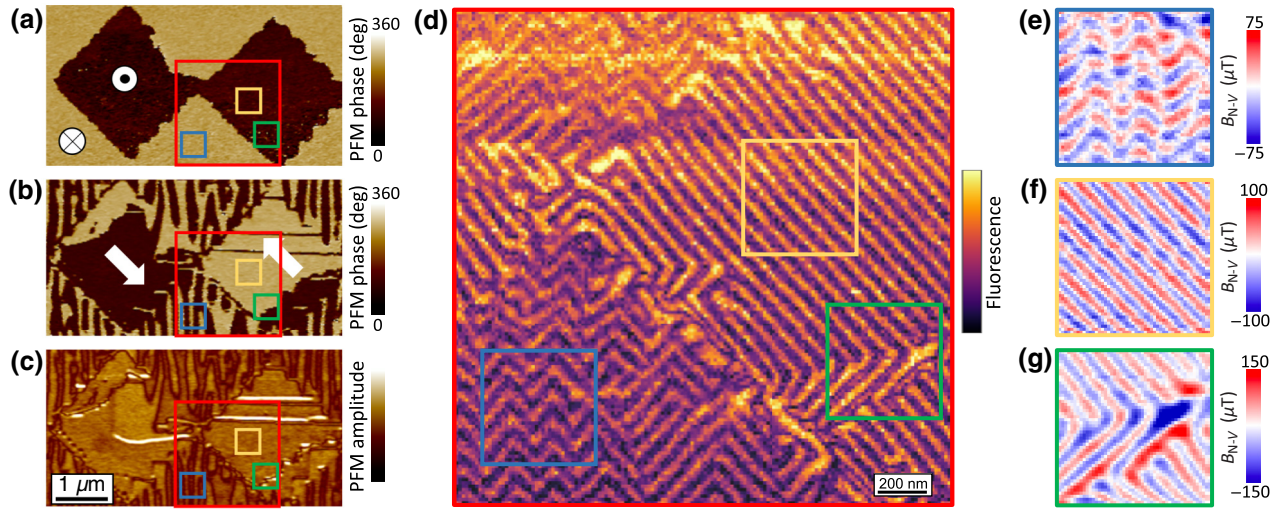


FIG. 3. Piezoresponse force microscopy (a) out-of-plane phase, (b) in-plane phase, and (c) in-plane amplitude images, showing two written ferroelectric domain areas containing a single out-of-plane variant and two in-plane ones. Red square indicates the area scanned in (d). (d) Large-area single iso-\$B\$ fluorescence image obtained with the scanning N-V magnetometer, with blue-, yellow-, and green-colored squares representing different areas collected in the quantitative imaging mode in (e)–(g), respectively.

at the edge of a transition to the pseudocollinear *G*-type antiferromagnetic state, the period diverges.

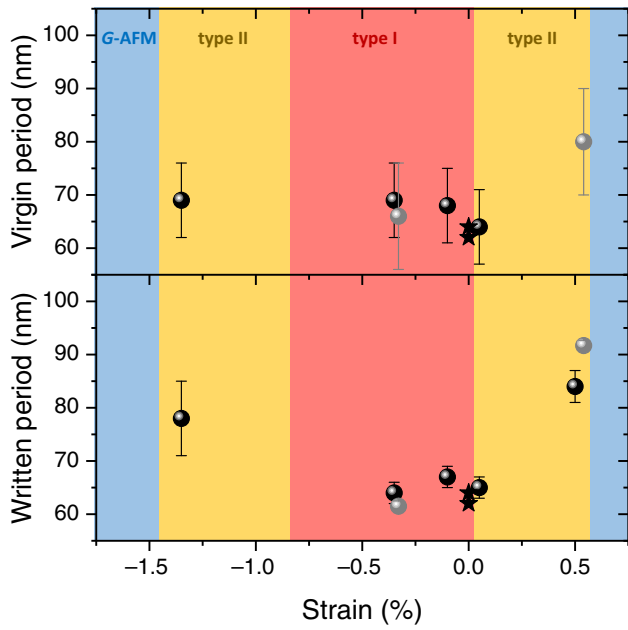


FIG. 4. Magnetic state versus strain phase diagram. Evolution of the spin-cycloid period measured as a function of strain in both the as-grown striped-domain state and written state are displayed in the upper and lower panels, respectively. Black dots are extracted from Refs. [14,23,24] and black stars represent bulk values from Refs. [2,3]. Gray dots are extracted from the present work. *G*-AFM stands for pseudocollinear *G*-type antiferromagnetic order.

Going further, we can extract the value of the DMI-induced uncompensated magnetic moments forming the spin-density wave from quantitative field maps. To achieve this, we perform additional quantitative measurements of the spin cycloid inside single written ferroelectric domains. As already shown in Fig. 3(f), we obtain a cycloid with a single propagation vector in these written zones, allowing us to fit experimental data with the analytical expression of the stray field generated by the spin-density wave and to extract the value of m_{DM} .

Figure 5(a) displays the map of the stray field produced by the type-I cycloid of a single ferroelectric domain of the BiFeO₃ thin film grown on DyScO₃. The propagation vector of the cycloid is perpendicular to the in-plane projection of polarization (which is parallel to the [111] direction), and therefore, corresponds to \vec{k}_1 , oriented along the [110] direction. In this configuration, the cycloid itself does not produce any magnetic stray field because of the compensation of the magnetic moments on the (001) surface. However, we are able to detect the spin-density wave, which we describe as

$$\vec{M}_{\text{SW}}(\vec{r}) = \frac{m_{\text{DM}}}{\sqrt{6}a^3} \cos(\vec{k}_1 \cdot \vec{r})(\hat{e}_x + \hat{e}_y - 2\hat{e}_z) \\ = \frac{m_{\text{DM}}}{\sqrt{6}a^3} \cos\left(\frac{k}{\sqrt{2}}(x-y)\right)(\hat{e}_x + \hat{e}_y - 2\hat{e}_z), \quad (1)$$

with $k = 2\pi/\lambda$, where λ is the cycloid period. To obtain an analytical expression of the stray field generated by the spin-density wave, we start by computing [13,25,26] the magnetic potential, Φ , for a single BiFeO₃ layer of thickness $a = 0.3965$ nm:

$$\phi(x, y, z) = -\frac{\mu_0}{4\pi} \int_{x'=-\infty}^{x'=\infty} \int_{y'=-\infty}^{y'=\infty} \int_{z'=-\alpha/2}^{z'=\alpha/2} \vec{M}_{\text{SW}}(x', y') \cdot \vec{\nabla}' \frac{1}{\sqrt{(x-x')^2 + (y-y')^2 + (z-z')^2}} dx' dy' dz'. \quad (2)$$

Since Φ is expressed as convolutions, we can compute it using two-dimensional Fourier transforms:

$$\begin{aligned} \mathcal{F}[\phi] = & -\frac{\mu_0}{4\pi} \int_{z'=-(\alpha/2)}^{z'=\alpha/2} \left\{ \mathcal{F}[M_x] \mathcal{F} \left[\frac{\partial}{\partial x} \frac{1}{R} \right] \right. \\ & \left. + \mathcal{F}[M_y] \mathcal{F} \left[\frac{\partial}{\partial y} \frac{1}{R} \right] + \mathcal{F}[M_z] \mathcal{F} \left[\frac{\partial}{\partial z} \frac{1}{R} \right] \right\} dz', \end{aligned} \quad (3)$$

where M_x , M_y , and M_z are the components of \vec{M}_{SW} and $1/R = 1/\sqrt{x^2 + y^2 + (z-z')^2}$. Next, we invert the Fourier transform and compute each term separately (see the Supplemental Material [27] for details of the calculations) to obtain the analytical expression of Φ :

$$\Phi = \frac{2\mu_0 m_{\text{DM}}}{\sqrt{6}a^3} \frac{e^{-kz}}{k} \sinh \left(\frac{ka}{2} \right) \cos \left(\frac{k}{\sqrt{2}}(x-y) \right). \quad (4)$$

The expression for the stray field, \vec{B} , for the whole film of thickness t results from $\vec{B} = -\vec{\nabla}\Phi$ and the sum of the field contributions from each BiFeO_3 layer. Finally, at a distance $z = d_{N-V}$ from the sample surface,

$$\begin{cases} B_x(x, y) = \mathcal{A} \sin \left(\frac{k}{\sqrt{2}}(x-y) \right), \\ B_y(x, y) = -\mathcal{A} \sin \left(\frac{k}{\sqrt{2}}(x-y) \right), \\ B_z(x, y) = \sqrt{2} \mathcal{A} \cos \left(\frac{k}{\sqrt{2}}(x-y) \right), \end{cases} \quad (5)$$

with

$$\mathcal{A} = \frac{\mu_0 m_{\text{DM}}}{\sqrt{3}a^3} e^{-kd_{N-V}} \frac{1 - e^{-kt}}{1 - e^{-ka}} \sinh \left(\frac{ka}{2} \right). \quad (6)$$

As shown in Fig. 5(b), we use the analytical expression [Eq. (5)] of the stray field arising from the spin-density wave tied to the type-I cycloid to fit the line profile extracted from our measurements on a 30-nm-thick film. Taking into account the calibration [Fig. 1(b)] of the N-V-to-sample distance, d_{N-V} , and the projection of the field along the N-V orientation direction (polar angle θ , azimuthal angle φ), we can evaluate the DMI-induced uncompensated magnetic moments, $m_{\text{DM}} = (0.51 \pm 0.13) \mu_B$, and the cycloid period, (61.5 ± 0.6) nm. This period is in agreement with the usually observed 64-nm cycloid period, whereas the uncompensated moments are significantly larger than that

measured in bulk BiFeO_3 ($0.06 \mu_B$) from neutron scattering experiments [4], indicating either a surface or a confinement effect. The large error in the determination of this parameter originates from the high sensitivity of \vec{B} to the value of d_{N-V} [see Eq. (6)]. See the Supplemental Material [27] for details of the estimation of the error.

We can repeat this procedure for the type-II cycloid in BiFeO_3 thin films grown on SmScO_3 , as shown in Figs. 5(b) and 5(d). We observe in the stray-field map that the projection of the propagation vector of the cycloid is almost parallel to the projection of the polarization, \vec{P} . Therefore, we assume that the cycloid propagates along \vec{k}'_3 , which is parallel to the $[11\bar{2}]$ direction. In this configuration, the spin-density wave is located in the surface plane:

$$\vec{M}_{\text{SW}}(\vec{r}) = \frac{m_{\text{DM}}}{\sqrt{2}a^3} \cos(\vec{k}'_3 \cdot \vec{r})(-\hat{e}_x + \hat{e}_y). \quad (7)$$

Such a magnetic state does not generate any magnetic stray field above the surface of the film [4], which is obviously in contradiction with our experimental results. We relate this to the misalignment between the projections of \vec{P} and \vec{k}'_3 , which was also found in previous experiments [14]. We take this into account by considering that the cycloid is rather propagating along $\vec{k}'_3(\alpha)$, which still lies in the plane perpendicular to \vec{P} , but deviates from \vec{k}'_3 by a small rotation angle, α . The geometrical relationship between α and the measurable angle, α_{proj} , indicated in Fig. 5(c) is

$$\tan \alpha_{\text{proj}} = -\sqrt{3} \tan \alpha. \quad (8)$$

The spin-density wave corresponding to this situation can be described as

$$\begin{cases} M_x = -\frac{m_{\text{DM}}}{\sqrt{6}a^3} (\sqrt{3} \cos \alpha + \sin \alpha) \cos[\vec{k}'_3(\alpha) \cdot \vec{r}], \\ M_y = \frac{m_{\text{DM}}}{\sqrt{6}a^3} (\sqrt{3} \cos \alpha - \sin \alpha) \cos[\vec{k}'_3(\alpha) \cdot \vec{r}], \\ M_z = \frac{2m_{\text{DM}} \sin \alpha}{\sqrt{6}a^3} \cos[\vec{k}'_3(\alpha) \cdot \vec{r}], \end{cases} \quad (9)$$

with

$$\begin{aligned} \vec{k}'_3(\alpha) = & \frac{2\pi}{\lambda\sqrt{6}} \left[(\cos \alpha - \sqrt{3} \sin \alpha) \hat{e}_x \right. \\ & \left. + (\cos \alpha + \sqrt{3} \sin \alpha) \hat{e}_y - 2 \cos \alpha \hat{e}_z \right]. \end{aligned} \quad (10)$$

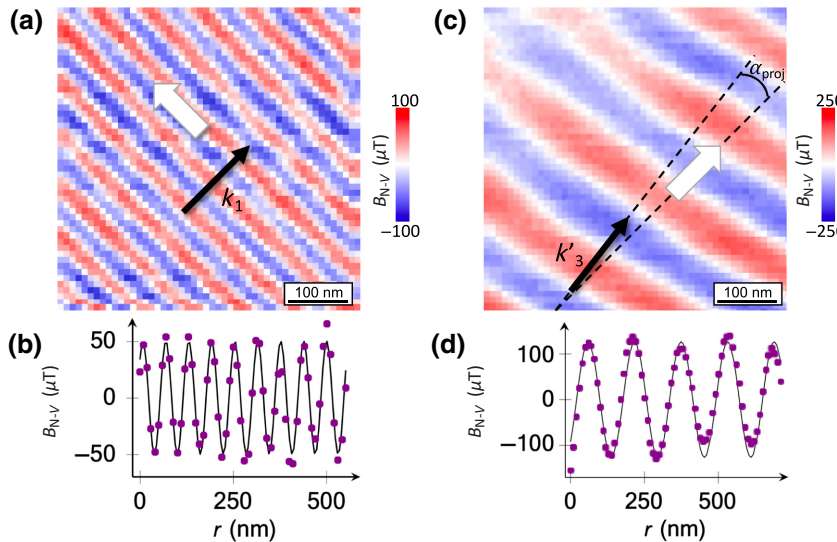


FIG. 5. (a) Quantitative stray-field map of the type-I cycloid in $\text{BiFeO}_3/\text{DyScO}_3$. (b) Extracted and fitted line profile of the type-I cycloid. (c) Quantitative stray-field map of the type-II cycloid in $\text{BiFeO}_3/\text{SmScO}_3$. (d) Extracted and fitted line profile of the type-II cycloid.

To compute Φ , we insert Eqs. (9) and (10) into Eq. (3) and we obtain, for a single BiFeO_3 layer,

$$\Phi = \frac{2\mu_0 m_{\text{DM}} \sin \alpha e^{-(\gamma kz/\sqrt{6})}}{k\gamma a^3} \sinh\left(\frac{\gamma ka}{2\sqrt{6}}\right) \cos[\vec{k}_3(\alpha) \cdot \vec{r}], \quad (11)$$

where

$$\gamma = \sqrt{\cos^2 \alpha + 3 \sin^2 \alpha}. \quad (12)$$

Summing again the field contributions for each single BiFeO_3 layer in the film of thickness t leads to the following expression of \vec{B} , at a distance d_{N-V} from the surface:

$$\begin{cases} B_x = \frac{A}{\gamma} (\cos \alpha - \sqrt{3} \sin \alpha) \text{Im}\{\mathcal{S}\}, \\ B_y = \frac{A}{\gamma} (\cos \alpha + \sqrt{3} \sin \alpha) \text{Im}\{\mathcal{S}\}, \\ B_z = A \left(\text{Re}\{\mathcal{S}\} - \frac{2 \cos \alpha}{\gamma} \text{Im}\{\mathcal{S}\} \right), \end{cases} \quad (13)$$

where

$$A = \frac{2\mu_0 m_{\text{DM}}}{\sqrt{6} a^3} \sin \alpha \sinh\left(\frac{\gamma ka}{2\sqrt{6}}\right) e^{-(\gamma kd_{N-V}/\sqrt{6})}, \quad (14)$$

and

$$\mathcal{S} = e^{i\vec{k}_3(\alpha) \cdot \vec{r}} \frac{1 - e^{-(kt/\sqrt{6})(\gamma + 2i\cos \alpha)}}{1 - e^{-(ka/\sqrt{6})(\gamma + 2i\cos \alpha)}}. \quad (15)$$

In the experiment presented in Fig. 5(c), we measure $\alpha = 4.5^\circ \pm 1^\circ$. Using again the probe calibration described in Fig. 1(b), we extract the values of m_{DM} and λ from a fit of the line profile in Fig. 5(d) to Eq. (13). We get smaller uncompensated magnetic moments than that for the type-I cycloid, $m_{\text{DM}} = (0.12 \pm 0.03) \mu_B$, and a significantly larger cycloid period, $(91.7 \pm 0.6) \text{ nm}$.

V. CONCLUSIONS

Using scanning N-V magnetometry, we are able to identify a critical epitaxial strain at which the cycloidal antiferromagnetic state of BiFeO_3 is on the brink of destabilization. While previous experiments suggested the presence of a pseudocollinear antiferromagnetic state with multiple domains for BiFeO_3 thin films grown on $\text{SmScO}_3(110)$ [14], here we observe that the cycloidal state is preserved while the period starts to diverge. Furthermore, we demonstrate that quantitative scanning N-V magnetometry provides insights into the physical parameters at play in antiferromagnetic cycloidal states. Coupling our measurement with analytical calculations of the expected stray field, we can even quantitatively characterize the spin-density wave, which is tied to the cycloid. For the bulklike spin cycloid with propagation vectors lying along the $[1\bar{1}0]$ direction, we extract a value of the uncompensated moment associated with the spin-density wave that is well beyond values reported for the bulk material. Regarding the exotic spin cycloid with propagation vectors lying along the $[11\bar{2}]$ direction, this uncompensated moment is 3 times lower and associated with a 4.5° shift of this propagation vector. These experiments suggest that scanning N-V magnetometry is a powerful tool to provide quantitative physical parameters in complex antiferromagnetic spin textures.

ACKNOWLEDGMENTS

We acknowledge support from the French Agence Nationale de la Recherche (ANR) through the PIAF and TATOO (Grant No. ANR-21-CE09-0033-01) projects. This work is supported by a public grant overseen by the ANR as part of the “Investissement d’Avenir” programme (LABEX NanoSaclay, Grant No. ANR-10-LABX-0035, Spicy). The Sesame Ile de France IMAGeSPIN project

(Grant No. EX039175) is also acknowledged. This project receives funding from the European Union's Horizon 2020 research and innovation programme under Grants No. 964931 (TSAR) and No. 866267 (EXAFONIS). P.M. acknowledges funding from the Swiss NSF Grant No. 188521.

-
- [1] D. Lebeugle, D. Colson, A. Forget, and M. Viret, Very large spontaneous electric polarization in BiFeO₃ single crystals at room temperature and Its evolution under cycling fields, *Appl. Phys. Lett.* **91**, 022907 (2007).
- [2] I. Sosnowska, T. P. Neumaier, and E. Steichele, Spiral magnetic ordering in bismuth ferrite, *J. Phys. C: Solid State Phys.* **15**, 4835 (1982).
- [3] D. Lebeugle, D. Colson, A. Forget, M. Viret, A. M. Bataille, and A. Gukasov, Electric-Field-Induced Spin Flop in BiFeO₃ Single Crystals at Room Temperature, *Phys. Rev. Lett.* **100**, 227602 (2008).
- [4] M. Ramazanoglu, M. Laver, W. Ratcliff, S. M. Watson, W. C. Chen, A. Jackson, K. Kothapalli, S. Lee, S.-W. Cheong, and V. Kiryukhin, Local Weak Ferromagnetism in Single-Crystalline Ferroelectric BiFeO₃, *Phys. Rev. Lett.* **107**, 207206 (2011).
- [5] A. K. Zvezdin, A. M. Kadomtseva, S. S. Krotov, A. P. Pyatakov, Yu. F. Popov, and G. P. Vorob'ev, Magnetoelectric interaction and magnetic field control of electric polarization in multiferroics, *J. Magn. Magn. Mater.* **300**, 224 (2006).
- [6] J. Buhot, C. Toulouse, Y. Gallais, A. Sacuto, R. de Sousa, D. Wang, L. Bellaiche, M. Bibes, A. Barthélémy, A. Forget, D. Colson, M. Cazayous, and M.-A. Measson, Driving Spin Excitations by Hydrostatic Pressure in BiFeO₃, *Phys. Rev. Lett.* **115**, 267204 (2015).
- [7] T. Zhao, A. Scholl, F. Zavaliche, K. Lee, M. Barry, A. Doran, M. P. Cruz, Y. H. Chu, C. Ederer, N. A. Spaldin, R. R. Das, D. M. Kim, S. H. Baek, C. B. Eom, and R. Ramesh, Electrical control of antiferromagnetic domains in multiferroic BiFeO₃ films at room temperature, *Nat. Mater.* **5**, 823 (2006).
- [8] L. Yin and W. Mi, Progress in BiFeO₃ -based heterostructures: Materials, properties and applications, *Nanoscale* **12**, 477 (2020).
- [9] C. Ederer and N. A. Spaldin, Weak ferromagnetism and magnetoelectric coupling in bismuth ferrite, *Phys. Rev. B* **71**, 060401 (2005).
- [10] F. Bai, J. Wang, M. Wuttig, J. Li, N. Wang, A. P. Pyatakov, A. K. Zvezdin, L. E. Cross, and D. Viehland, Destruction of spin cycloid in (111)c-oriented BiFeO₃ thin films by epitaxial constraint: Enhanced polarization and release of latent magnetization, *Appl. Phys. Lett.* **86**, 032511 (2005).
- [11] X. Ke, P. P. Zhang, S. H. Baek, J. Zarestky, W. Tian, and C. B. Eom, Magnetic structure of epitaxial multiferroic BiFeO₃ films with engineered ferroelectric domains, *Phys. Rev. B* **82**, 134448 (2010).
- [12] D. Sando, *et al.*, Crafting the magnonic and spintronic response of BiFeO₃ films by epitaxial strain, *Nat. Mater.* **12**, 641 (2013).
- [13] I. Gross, W. Akhtar, V. Garcia, L. J. Martínez, S. Chouaieb, K. Garcia, C. Carrétéro, A. Barthélémy, P. Appel, P. Maletinsky, J.-V. Kim, J. Y. Chauleau, N. Jaouen, M. Viret, M. Bibes, S. Fusil, and V. Jacques, Real-Space imaging of Non-collinear antiferromagnetic order with a single-spin magnetometer, *Nature* **549**, 252 (2017).
- [14] A. Haykal, J. Fischer, W. Akhtar, J.-Y. Chauleau, D. Sando, A. Finco, F. Godel, Y. A. Birkhölzer, C. Carrétéro, N. Jaouen, M. Bibes, M. Viret, S. Fusil, V. Jacques, and V. Garcia, Antiferromagnetic textures in BiFeO₃ controlled by strain and electric field, *Nat. Commun.* **11**, 1704 (2020).
- [15] L. Rondin, J.-P. Tetienne, T. Hingant, J.-F. Roch, P. Maletinsky, and V. Jacques, Magnetometry with nitrogen-vacancy defects in diamond, *Rep. Prog. Phys.* **77**, 056503 (2014).
- [16] U. Celano, H. Zhong, F. Ciubotaru, L. Stoleriu, A. Stark, P. Rickhaus, F. F. de Oliveira, M. Munsch, P. Favia, M. Korytov, P. Van Marcke, P. Maletinsky, C. Adelmann, and P. van der Heide, Probing magnetic defects in ultra-scaled nanowires with optically detected spin resonance in nitrogen-vacancy center in diamond, *Nano Lett.* **21**, 10409 (2021).
- [17] T. Hingant, J.-P. Tetienne, L. J. Martínez, K. Garcia, D. Ravelosona, J.-F. Roch, and V. Jacques, Measuring the Magnetic Moment Density in Patterned Ultrathin Ferromagnets with Submicrometer Resolution, *Phys. Rev. Appl.* **4**, 014003 (2015).
- [18] A. Haykal, A. Finco, S. Fusil, P. Kumar, J.-Y. Chauleau, M. Viret, N. Jaouen, V. Garcia, and V. Jacques, Imaging Topological Defects in a Non-Collinear Antiferromagnet, *Phys. Rev. Lett.* (2022) arXiv:2202.02243.
- [19] Z. H. Chen, A. R. Damodaran, R. Xu, S. Lee, and L. W. Martin, Effect of “symmetry mismatch” on the domain structure of rhombohedral BiFeO₃ thin films, *Appl. Phys. Lett.* **104**, 182908 (2014).
- [20] Y. Nahas, S. Prokhorenko, J. Fischer, B. Xu, C. Carrétéro, S. Prosandeev, M. Bibes, S. Fusil, B. Dkhil, V. Garcia, and L. Bellaiche, Inverse transition of labyrinthine domain patterns in ferroelectric thin films, *Nature* **577**, 47 (2020).
- [21] N. Balke, S. Choudhury, S. Jesse, M. Huijben, Y. H. Chu, A. P. Baddorf, L. Q. Chen, R. Ramesh, and S. V. Kalinin, Deterministic control of ferroelastic switching in multiferroic materials, *Nat. Nanotechnol.* **4**, 868 (2009).
- [22] A. Crassous, T. Sluka, A. K. Tagantsev, and N. Setter, Polarization charge as a reconfigurable quasi-dopant in ferroelectric thin films, *Nat. Nanotechnol.* **10**, 614 (2015).
- [23] A. Haykal, PhD thesis, Université de Montpellier 2020.
- [24] J. Fischer, PhD thesis, Université Paris-Saclay 2020.
- [25] R. J. Blakely, *Potential Theory in Gravity and Magnetic Applications* (Cambridge University Press, Cambridge, 1995).
- [26] N. Mikuszeit, S. Meckler, R. Wiesendanger, and R. Miranda, Magnetostatics and the rotational sense of cycloidal spin spirals, *Phys. Rev. B* **84**, 054404 (2011).
- [27] See the Supplemental Material at <http://link.aps.org/supplemental/10.1103/PhysRevApplied.17.044051> for details of the analytical calculations and of the estimation of the errors on the uncompensated moment of the spin density wave.